SUPPLEMENTARY NOTE 1: METHODS

Sample Preparation

We have prepared polished single crystals of UO_2 oriented within 0.1° of the (001) and (111) surface planes, as described elsewhere.[1] The (111) sample was an unoxidized control. The (001) sample was exposed to 1 atm of dry oxygen gas for 21 days at room-temperature and measured on the GSECARS Beamlines 13-IDC and 13-BMC at the Advanced Photon Source, Argonne National Laboratory.[2] It was subsequently stored in air for several months at room-temperature prior to STEM preparation.

STEM Imaging

Cross-sectional STEM samples were prepared using an FEI Helios NanoLab DualBeam Focused Ion Beam (FIB) microscope and a standard lift out procedure along the UO_2 [100] and [110] zone-axes for the (001)-oriented and (111)-oriented samples, respectively. Initial cuts were made at 30 kV / 1.5° and final polishing at 2 kV / 2.5° ion beam energy / incidence angles. Images and fine structure maps were collected on a probe-corrected JEOL ARM-200CF microscope operating at 200 kV accelerating voltage, with a probe semi-convergence angle of 27.5 mrad, a HAADF collection angle of 82–186 mrad, and a EELS inner collection angle of 42.9 mrad. EELS fine structure maps were collected using a 1 Å probe size with a $\sim$ 130 pA probe current and a 0.25 eV ch^{-1} dispersion, yielding an effective energy resolution of $\sim$ 0.75 eV. The O K edge spectra were corrected for energy drift using the zero-loss peak, then treated with a power low background subtraction fit to a 60 eV window prior to the edge, and processed using a Fourier-Ratio deconvolution. The extracted spectra were integrated within windows parallel to the sample surface to improve signal-to-noise, as marked in main text Fig. 2. Separate composition maps were collected on a probe-corrected JEOL ARM-300F microscope operating at 300 kV accelerating voltage, with a probe semi-convergence angle of 28 mrad and a EELS inner collection angle of 87 mrad with a 1 Å probe size with a $\sim$ 260 pA probe current and a 1 eV ch^{-1} dispersion. To improve signal-to-noise, the spectrometer was binned 4× in the energy axis.

Multislice Simulations

We have performed STEM image simulations to determine the effect of interstitial and total oxygen on the STEM-HAADF image intensity for UO_2 along the [100] zone-axis. These image simulations were performed using the PRISM method described in Ref. 3, implemented in the Prismatic software described in Ref. 4. An accelerating voltage of 200 kV, a probe semi-convergence angle of 27.5 mrad, and HAADF collection angles of 82–186 mrad were set to match the experimental parameters. An in-plane pixel sampling of 0.0337 Å and a slice thickness of 1.3678 Å were used. A total thickness of 60 nm was used for all simulations, with an in-plane tiling of 5×5 UO_2 unit cells to minimize probe wrap-around errors. 25 frozen phonon configurations were used to include thermal scattering effects. A PRISM interpolation factor of 1 was used in the x and y directions, making the simulation mathematically identical to the multislice method.[3] The atomic scattering potentials used and more information about the multislice method are given in Ref. 5. The oxygen concentration was independently varied on two sublattice sites—the bulk structure and interstitial sites—for total stoichiometries from UO_2 to UO_3, shown in Fig. S4.

Density Functional Theory Calculations

In this study, two set of computational simulations were performed. First, the defect-free and defective crystal structures of UO_2 were optimized in the density functional theory (DFT) framework, as implemented in the VASP package,[6,7] with the generalized gradient approximation (GGA) and the Perdew-Burke-Ernzerhof (PBE) parametrization[8] exchange-correlation functional. In each calculation, the cutoff energy of the projector augmented wave[9] pseudo-potential was 600 eV and a Gamma centered k-points mesh of $6 \times 6 \times 6$ for the sampling of the Brillouin zone was used. The total energy was converged to 10^{-5} eV cell^{-1} and the force components were relaxed to below 10^{-3} eV Å^{-1}. Spin-polarization and the Vosko-Wilk-Nusair local density approximation scheme[10] were used. The GGA+U method, as described by Dudarev,[11] was used for the U atoms to correct the description of the Coulomb repulsion of the $5f$ electrons in standard GGA. The Hubbard parameter, U, describing the Coulomb interaction, was fixed to 4.5 eV, while the screened exchange energy, J, was fixed to 0.51 eV.[12] Subsequently, we used the relaxed defect-free and defective supercell to calculate the O K edge XANES spectra with the FDMNES code.[13] Although EELS and

XANES are not strictly equivalent techniques, they probe the same electronic states. Therefore, a comparison between experimental and theoretical spectra across the two techniques provide invaluable insight and are commonly used to rationalize observed trends and fine structure features in oxides.[14] In FDMNES, the final excited state is obtained by solving a Schrödinger-like equation through the Greens formalism, within the limit of the muffin-tin approximation. The potentials and Fermi energy were determined self-consistently using a radii of 7 Å. Similar radii were used for the calculations of the spectra. Real Hedin-Lundquist potentials[15] were used to model the exchange-correlation. Dipoles, quadrupoles, core-hole and spin-orbit contributions were taken into account. All the DFT calculations used a 2×2 (111) hexagonal unit cell of UO_2 containing 12× U and 24× O atoms. The position of the interstitial O atom in this unit cell was identical to the one proposed in Ref. 1 and is shown in Fig. S9.

SUPPLEMENTARY NOTE 2: UNIFORMITY OF SURFACE OXIDATION

We have measured multiple regions of the oxidized (001) sample and confirm the presence of a uniform, high-contrast band at the surface. Moreover, we observe minimal long-range defects and impurities, reflecting the high quality of the sample.

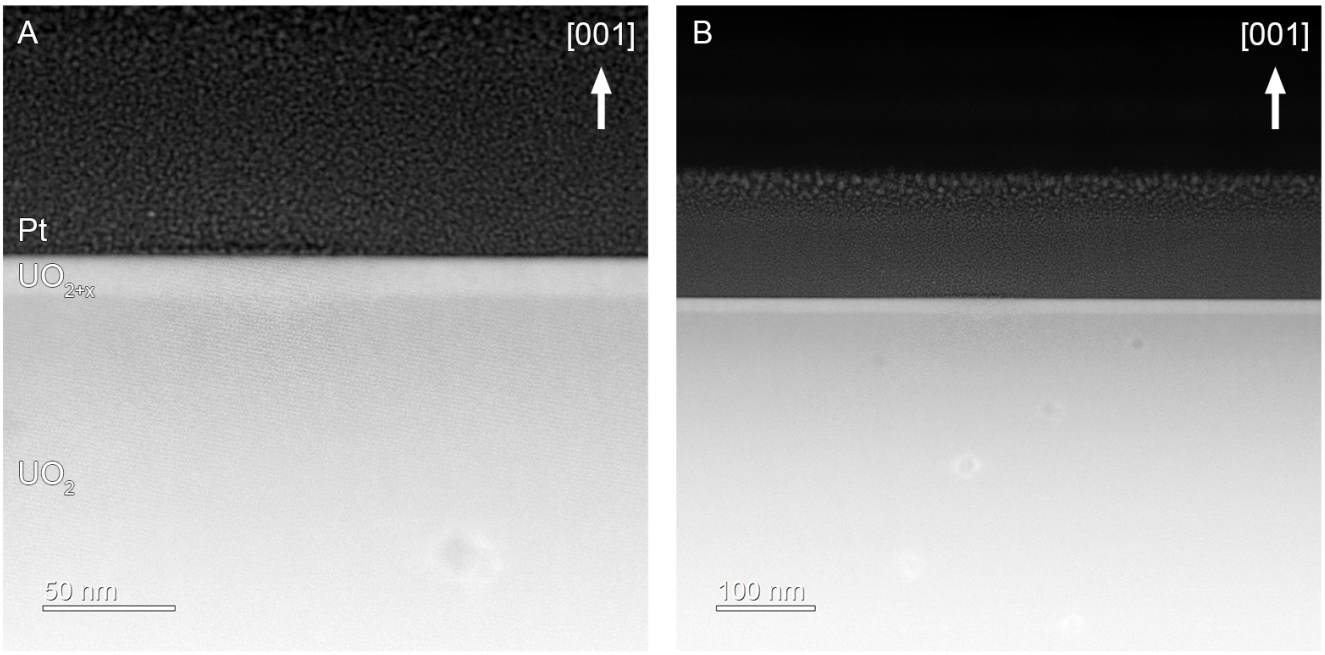

FIG. S1. (A) Representative intermediate- and (B) low-magnification cross-sectional STEM-HAADF images of the (001) sample.

SUPPLEMENTARY NOTE 3: ELECTRON ENERGY LOSS SPECTROSCOPY THICKNESS MAPPING

To assess the possibility of local thickness variations, we have performed EELS thickness mapping of the surface band in the (001) sample. We find that the sample varies from 55–60 nm and that no abrupt change in thickness occurs that might indicate carbon contamination or lattice bending.

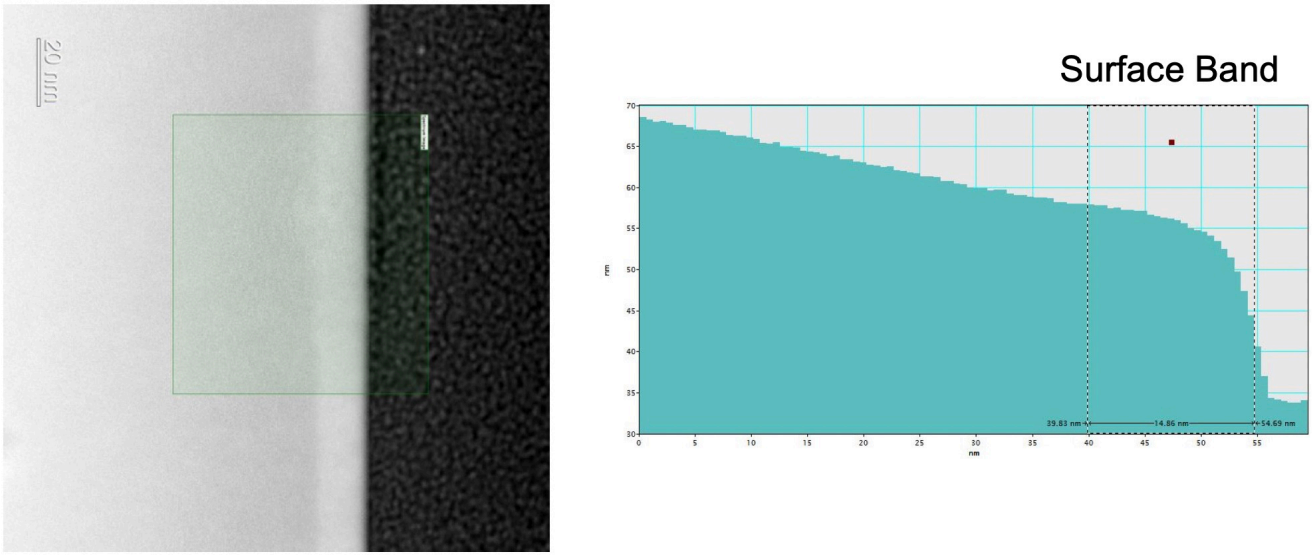

FIG. S2. (Left) STEM-HAADF image of the (001) sample and (Right) associated STEM-EELS thickness map.

SUPPLEMENTARY NOTE 4: GEOMETRIC PHASE ANALYSIS STRAIN MAPPING

We confirm the nominal UO_2 fluorite crystal structure for both samples shown in the main text. The (111) sample has experimentally measured reciprocal lattice vectors of $\mathbf{g}_{[1\bar{1}\bar{1}]} = 0.314$ Å^{-1}, $\mathbf{g}_{[00\bar{2}]} = 0.362$ Å^{-1}, $\mathbf{g}_{[\bar{1}1\bar{1}]} = 0.514$ Å^{-1} versus expected bulk values of $\mathbf{g}_{[1\bar{1}\bar{1}]} = 0.318$ Å^{-1}, $\mathbf{g}_{[00\bar{2}]} = 0.367$ Å^{-1}, $\mathbf{g}_{[\bar{1}1\bar{1}]} = 0.519$ Å^{-1}.[16] The (001) sample has experimentally measured reciprocal lattice vectors of $\mathbf{g}_{[200]} = 0.363$ Å^{-1}, $\mathbf{g}_{[0\bar{2}0]} = 0.362$ Å^{-1}, $\mathbf{g}_{[2\bar{2}0]} = 0.514$ Å^{-1} versus expected bulk values of $\mathbf{g}_{[200]} = 0.367$ Å^{-1}, $\mathbf{g}_{[0\bar{2}0]} = 0.367$ Å^{-1}, $\mathbf{g}_{[2\bar{2}0]} = 0.519$ Å^{-1}.

To explore the local variation in strain state, we have performed geometric phase analysis (GPA) using the FRWR-tools plugin developed by Cristoph Koch.[17] In theory, GPA is capable of measuring lattice strains at the sub-nanometer length scale, with better than 0.1% strain resolution.[18,19] However, the technique is prone to stripe-like artifacts resulting from scan distortions in STEM,[20] so we have collected a series of drift-corrected images using the SmartAlign plugin, which are subsequently rigid-aligned and averaged.[21] Fig. S3 shows the imaged region, diffraction pattern, and corresponding in- and out-of-plane strain maps. While some random variations are present in the data, we observe no clear and systematic lattice distortion in the surface region that might indicate lattice bending or a large-scale phase transformation. This result is not surprising, considering the small expected strains and possible local variations associated with oxygen interstitial incorporation.

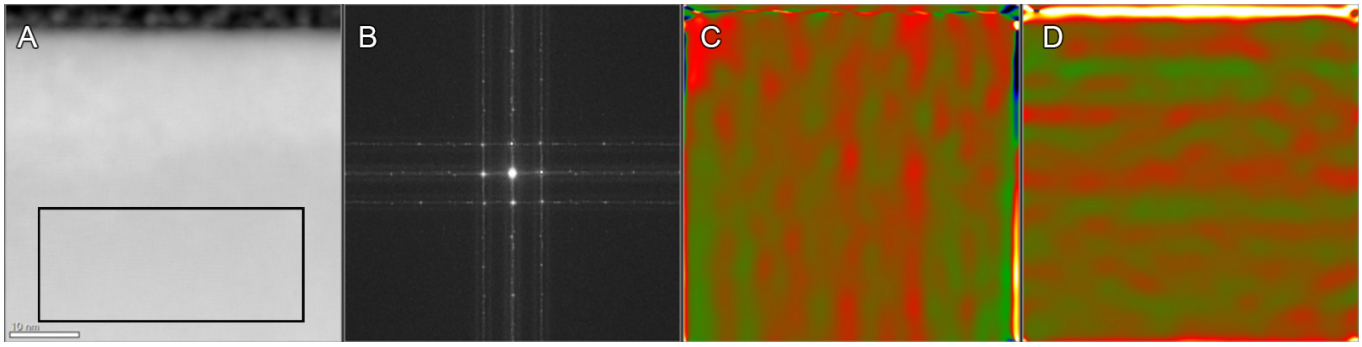

FIG. S3. (A) Rigid-aligned STEM-HAADF image, (B) Corresponding diffraction pattern, (C) In-plane strain component (ϵ_{xx}) and (D) Out-of-plane strain component (ϵ_{yy}). The rectangle indicates the reference lattice.

SUPPLEMENTARY NOTE 5: MULTISLICE SIMULATIONS OF INTERSTITIAL OXYGEN

We have performed an array of multislice simulations for a range of different fractional lattice and oxygen site occupancies, as shown in Fig. S4. We find that there are pronounced differences in image contrast that can be accounted for primarily by the increased scattering cross section caused by excess interstitial oxygen. The mean intensity of each STEM-HAADF image is given as percentage of the total probe current, and the relative percentage change from the bulk UO_2 signal is shown in brackets. Excess oxygen in the interstitial sites also shortens the channeling length along the U + interstitial O columns, as shown in Fig. S5. Additional channeling contrast along adjacent atomic columns is also visible. These simulations confirm that the observed experimental contrast change can be achieved through the incorporation of excessive interstitial oxygen.

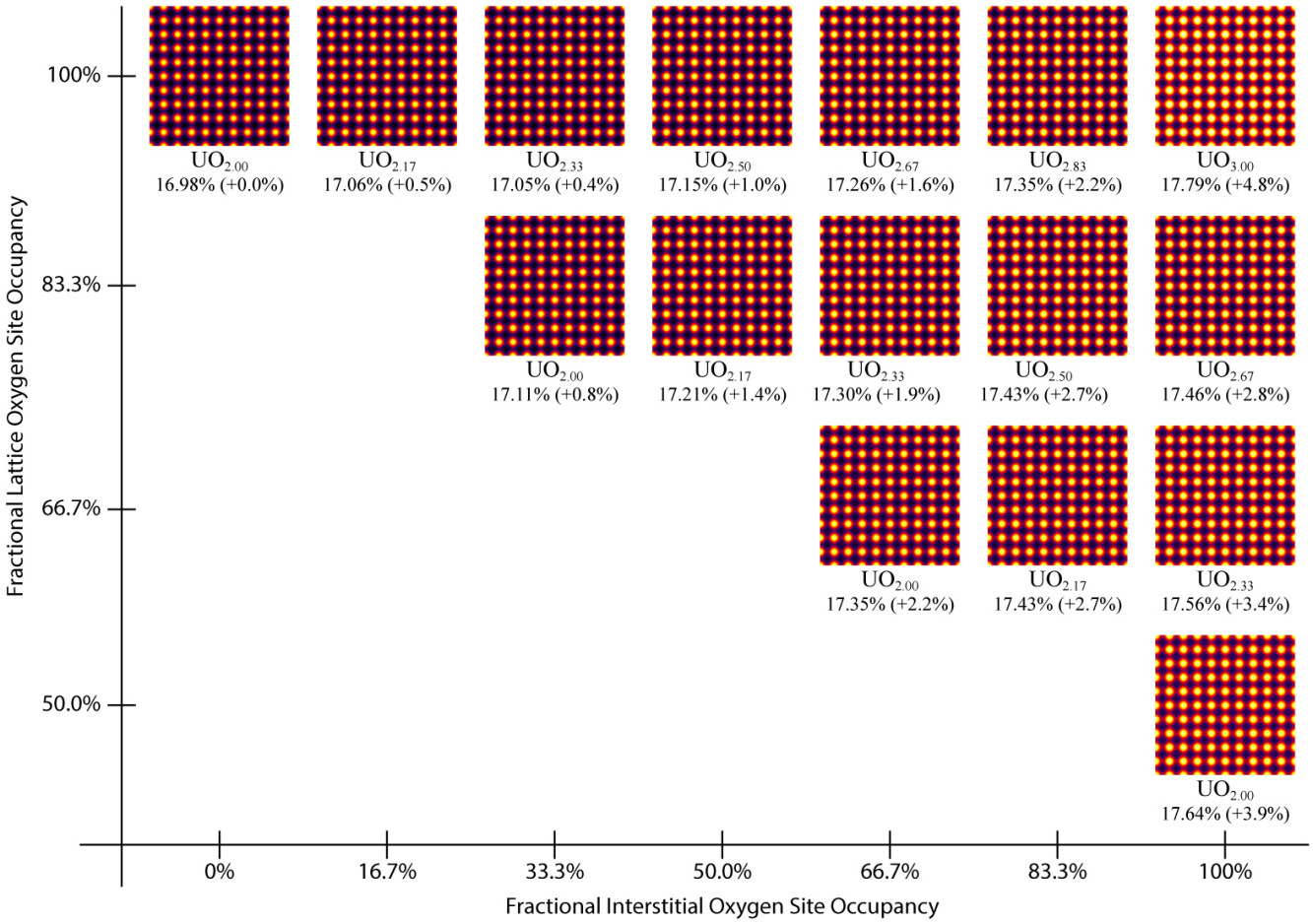

FIG. S4. Table of image simulations for different lattice and fractional interstitial oxygen site occupancies.

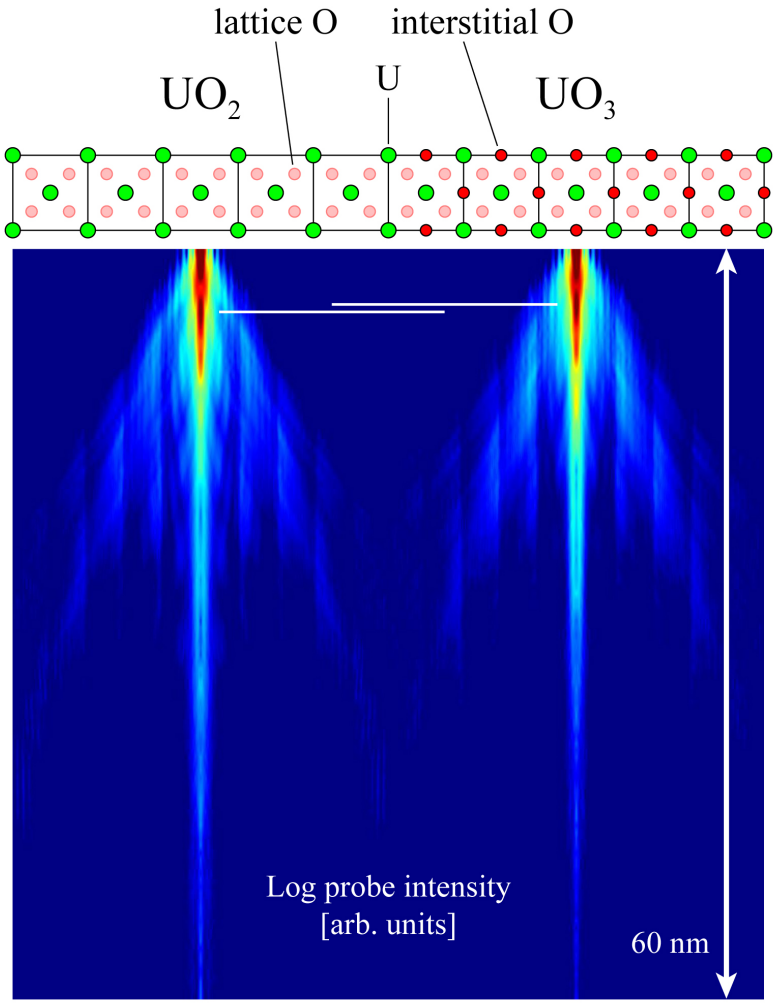

FIG. S5. Calculated differences in electron probe scattering for UO_2 and UO_3.

SUPPLEMENTARY NOTE 6: DETAILS OF DENSITY FUNCTIONAL THEORY CALCULATIONS

Figure S6 shows a comparison between the calculated and measured UO_2 EELS spectra measured deep in the bulk of the unoxidized (111) sample. Figure S7 compares the spectral modifications induced by O interstitials and vacancies. While O vacancies can reduce the intensity of peak **2**, they affect the intensity of the minimum in between peak **1** and **2** to a lesser degree than interstitial O, and have no noticeable effects on the post-peak **2** shoulder. The effects of uniform lattice expansion and contraction are anti-correlated, as shown in Fig. S8. While lattice contraction can reduce the relative intensity of peak **2** with respect to peak **1**, it does not fill the minimum in between those peaks. Finally, Figure S9 shows the particular lattice and defect representation used in our calculations.

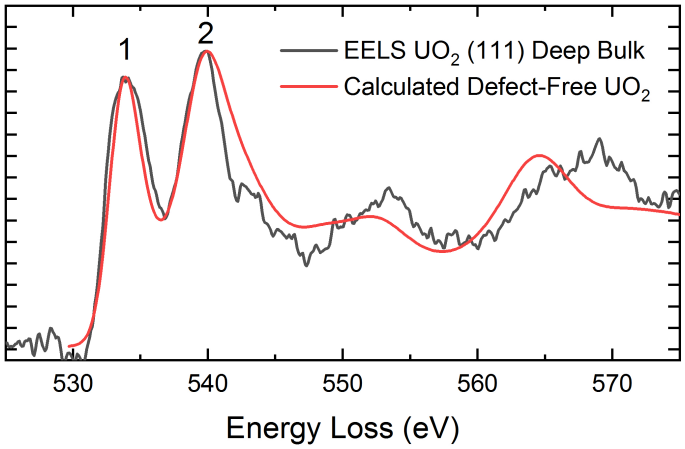

FIG. S6. Comparison between experimental O K edge spectrum of UO_2 taken deep in the bulk (∼100 nm from surface) of the (111) sample and the calculated spectrum for a defect-free UO_2 lattice.

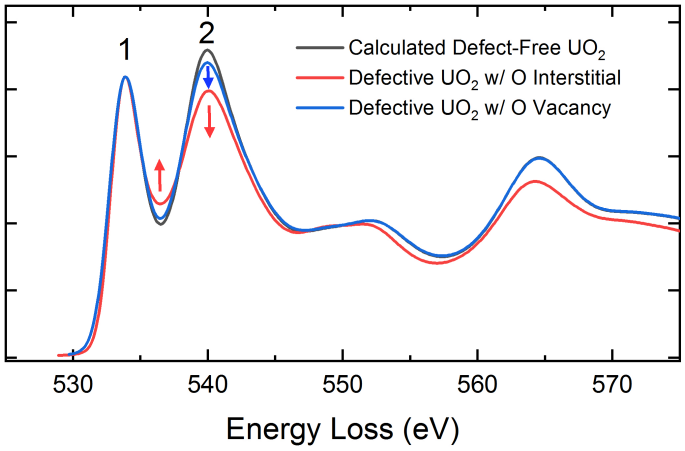

FIG. S7. Comparison of the spectral changes associated with an oxygen interstitial and vacancy.

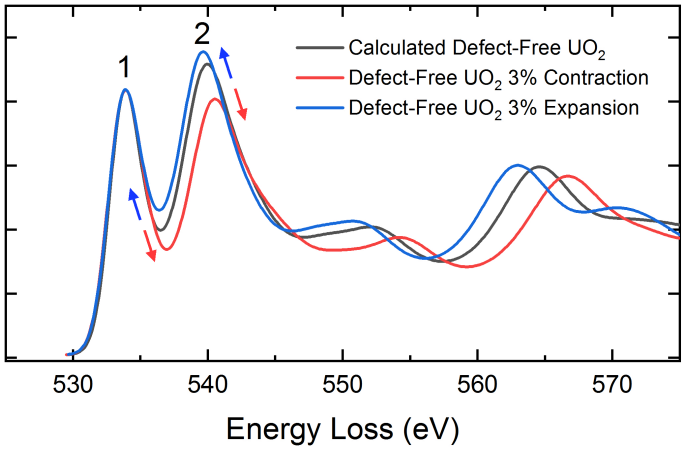

FIG. S8. Comparison of the spectral changes associated with homogeneous lattice expansion and contraction of a, b, and c lattice parameters of cubic UO_2.

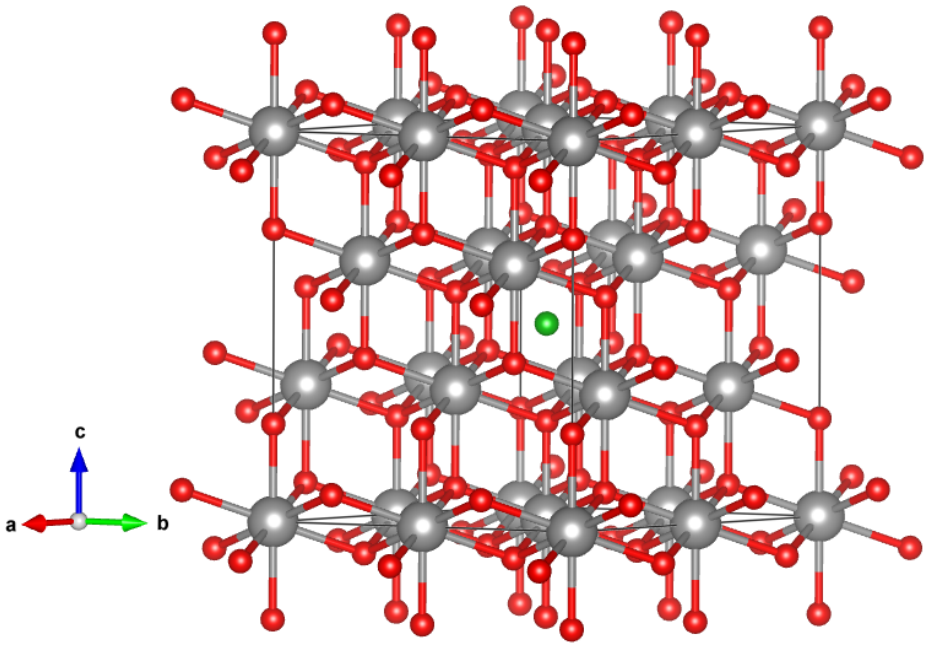

FIG. S9. Representation of interstitial O in UO_2 after relaxation by DFT calculations.

SUPPLEMENTARY REFERENCES

[1] Joanne E. Stubbs, Anne M. Chaka, Eugene S. Ilton, Craig A. Biwer, Mark H. Engelhard, John R. Bargar, and Peter J. Eng, "UO2 Oxidative Corrosion by Nonclassical Diffusion," Phys. Rev. Lett. **114**, 246103 (2015).

[2] Joanne E. Stubbs, Craig A. Biwer, Anne M. Chaka, Eugene S. Ilton, Yingge Du, John R. Bargar, and Peter J. Eng, "Oxidative Corrosion of the UO2(001) Surface by Nonclassical Diffusion," Langmuir **33**, 13189–13196 (2017).

[3] Colin Ophus, "A fast image simulation algorithm for scanning transmission electron microscopy," Advanced Structural and Chemical Imaging **3**, 13 (2017), arXiv:1702.01904.

[4] Alan Pryor, Colin Ophus, and Jianwei Miao, "A Streaming Multi-GPU Implementation of Image Simulation Algorithms for Scanning Transmission Electron Microscopy," Advanced Structural and Chemical Imaging (2017), 10.1186/s40679-017-0048-z, arXiv:1706.08563.

[5] Earl J. Kirkland, *Advanced Computing in Electron Microscopy* (Springer US, Boston, MA, 2010).

[6] G. Kresse and J. Furthmüller, "Efficiency of ab-initio total energy calculations for metals and semiconductors using a plane-wave basis set," Comput. Mater. Sci. **6**, 15–50 (1996).

[7] G. Kresse and J. Furthmüller, "Efficient iterative schemes for ab initio total-energy calculations using a plane-wave basis set," Phys. Rev. B **54**, 11169–11186 (1996).

[8] John P. Perdew, Kieron Burke, and Matthias Ernzerhof, "Generalized Gradient Approximation Made Simple," Phys. Rev. Lett. **77**, 3865–3868 (1996).

[9] P. E. Blöchl, "Projector augmented-wave method," Phys. Rev. B **50**, 17953–17979 (1994).

[10] S. H. Vosko, L. Wilk, and M. Nusair, "Accurate spin-dependent electron liquid correlation energies for local spin density calculations: a critical analysis," Can. J. Phys. **58**, 1200–1211 (1980).

[11] S. L. Dudarev, G. A. Botton, S. Y. Savrasov, Z. Szotek, W. M. Temmerman, and A. P. Sutton, "Electronic Structure and Elastic Properties of Strongly Correlated Metal Oxides from First Principles: LSDA + U, SIC-LSDA and EELS Study of UO2 and NiO," Phys. status solidi **166**, 429–443 (1998).

[12] Boris Dorado, Bernard Amadon, Michel Freyss, and Marjorie Bertolus, "DFT + U calculations of the ground state and metastable states of uranium dioxide," Phys. Rev. B **79**, 235125 (2009).

[13] O Bunu and Y Joly, "Self-consistent aspects of x-ray absorption calculations," Journal of Physics: Condensed Matter **21**, 345501 (2009).

[14] Steven R. Spurgeon, Prasanna V. Balachandran, Despoina M. Kepaptsoglou, Anoop R. Damodaran, J. Karthik, Siamak Nejati, Lewys Jones, Haile Ambaye, Valeria Lauter, Quentin M. Ramasse, Kenneth K.S. Lau, Lane W. Martin, James M. Rondinelli, and Mitra L. Taheri, "Polarization screening-induced magnetic phase gradients at complex oxide interfaces," Nat. Commun. **6**, 6735 (2015).

[15] L Hedin and B I Lundqvist, "Explicit local exchange-correlation potentials," J. Phys. C Solid State Phys. **4**, 2064–2083 (1971).

[16] B. Wasserstein, "Ages of Uraninites by a New Method," Nature **174**, 1004–1005 (1954).

[17] C.T. Koch, *Determination of core structure periodicity and point defect density along dislocations*, Ph.D. thesis, Arizona State University (2002).

[18] Martin J. Hÿtch and Andrew M. Minor, "Observing and measuring strain in nanostructures and devices with transmission electron microscopy," MRS Bull. **39**, 138–146 (2014).

[19] M.J. Hÿtch and F. Houdellier, "Mapping stress and strain in nanostructures by high-resolution transmission electron microscopy," Microelectron. Eng. **84**, 460–463 (2007).

[20] Maryam Vatanparast, Per Erik Vullum, Magnus Nord, Jian-Min Zuo, Turid W. Reenaas, and Randi Holmestad, "Strategy for reliable strain measurement in InAs/GaAs materials from high-resolution Z-contrast STEM images," J. Phys. Conf. Ser. **902**, 012021 (2017).

[21] Lewys Jones, Hao Yang, Timothy J. Pennycook, Matthew S. J. Marshall, Sandra Van Aert, Nigel D. Browning, Martin R. Castell, and Peter D. Nellist, "Smart Align—a new tool for robust non-rigid registration of scanning microscope data," Adv. Struct. Chem. Imaging **1**, 8 (2015).